Phase Reentrances and Solid Deformations in Confined Colloidal Crystals

Xiaoxia Li[1,2,*], Huang Fang[1,*], Krongtum Sankaewtong[3,*], Minhuan Li[1], Yanshuang Chen[1], Jiping Huang[1], Ran Ni[3,†], Hajime Tanaka[4,5,‡] and Peng Tan[1,2,§]

[1]*State Key Laboratory of Surface Physics and Department of Physics, Fudan University, Shanghai 200433, China*
[2]*Institute for Nanoelectronic Devices and Quantum Computing, Fudan University, Shanghai 200433, China*
[3]*Chemical Engineering, School of Chemical and Biomedical Engineering,*
Nanyang Technological University, 62 Nanyang Drive, 637459, Singapore
[4]*Department of Fundamental Engineering, Institute of Industrial Science,*
University of Tokyo, 4-6-1 Komaba, Meguro-ku, Tokyo 153-8505, Japan
[5]*Research Center for Advanced Science and Technology, University of Tokyo, 4-6-1 Komaba, Meguro-ku, Tokyo 153-8904, Japan*

A simple geometric constraint often leads to novel, complex crystalline phases distinct from the bulk. Using thin-film charge colloidal crystals, a model system with tunable interactions, we study the effects of geometric constraints. Through a combination of experiments and simulations, we systematically explore phase reentrances and solid deformation modes concerning geometrical confinement strength, identifying two distinct categories of phase reentrances below a characteristic layer number, N_c: one for bcc bulk-stable and another for fcc bulk-stable systems. We further verify that the dominant thermodynamic origin is the nonmonotonic dependence of solids' free energy on the degree of spatial confinement. Moreover, we discover transitions in solid deformation modes between interface-energy and bulk-energy dominance: below a specific layer number, N_k, geometric constraints generate unique soft deformation modes adaptive to confinement. These findings on the N-dependent thermodynamic and kinetic behaviors offer fresh insights into understanding and manipulating thin-film crystal structures.

Phase reentrances denote the recurrent emergence of phases in specific sequences as thermodynamic conditions, such as density or temperature, vary. This phenomenon is observed across various material classes, ranging from hard ceramics to soft hydrogels, proving to be a reliable method for finely controlling phase behaviors [1]. Besides density and temperature, geometrical constraints significantly alter phase behaviors [2–5]. For instance, a thin crystalline film between two parallel flat substrates undergoes a transition in crystalline order and physical properties between three-dimensional (3D) and two-dimensional (2D) limits [6]. This transition can lead to exotic crystalline phases distinct from those observed in bulk materials. Thus, when geometric constraints induce phase reentrances, intriguing material properties are expected, spanning many classes of thin-film solids and nanocrystalline particles with unique structures and properties. Despite the technological importance of these phenomena, the rules governing reentrance and the transition point from bulk to constrained states still remain elusive due to their inherent complexity and diversity.

The simplest example of such confinement is one-dimensional (1D) confinement within a 3D system. For example, when a hard-sphere colloidal crystal is confined between two parallel flat walls, cascades of thin-film crystals, such as multilayer square and hexagonal structures, may repeatedly emerge. The activation of phase-reentrance behavior occurs below a characteristic number of particle layers, N_c, signifying the transition from quasi-two-dimensional (quasi-2D) to bulk 3D behaviors [7–13]. This behavior in hard-sphere systems has been comprehensively explained by an entropic effect [7–10].

Furthermore, in systems with soft, anisotropic, or long-range interactions, complex solid structures induced by confinement have been robustly observed [13–20]. These studies indicate that constraint-induced multiple reentrances are a universal phenomenon. Thus, the presence or absence of phase reentrances can be conceptualized as a thermodynamic "magic layer number" phenomenon. However, a systematic experimental study on the impact of interparticle interaction nature on this phenomenon is still lacking.

In addition to producing complex phase reentrances, the constraint also induces transitions in the kinetics of phase transitions from bulk to constrained conditions. The kinetic behavior dependent on the layer number (N) was observed in geometrically constrained thin-film systems: the pathways of melting, crystallization, and solid-to-solid transitions critically depend on the layer number N [21–27]. Moreover, these studies indicate that the thermal and mechanical response of a thin-film state, adaptive to confinement, is distinct from both the 2D and 3D cases. It exhibits a unique character sensitive to the strength of the constraint. This behavior can be attributed

to a dimensionality specific effect in 2D, arising from the impact of thermal fluctuations on ordering, known as the Mermin-Wagner effect [28]. Despite the significance of phase transition kinetics in understanding the magic layer number puzzles, the dynamic behaviors of constrained thin films—specifically, how the solids deform adaptively to the constraint—and the possible underlying mechanism remain a significant mystery.

To address these fundamental issues, we employ charged colloidal systems with tunable interaction potentials. Colloidal systems provide a means to observe dynamic responses at the single-particle level under spatial confinement, offering a microscopic understanding of various phase behaviors such as crystallization [29–32], melting [22,23], premelting [21,25], and solid-solid transitions [24,27]. Through a combination of experiments and simulations on charged colloidal thin-film systems, we have identified two categories of phase reentrances induced by geometric constraints below a characteristic layer number, N_c: one for bcc bulk-stable and another for fcc bulk-stable systems. More importantly, we have identified transitions in solid deformation modes, termed constraint-to-bulk transitions, between interface-energy and bulk-energy dominance in thin-film states: below a critical layer number N_k, geometric constraints give rise to unique soft deformation modes that adapt to the confinement.

We use a density- and refractive-index-matched colloidal suspension with a particle volume fraction, $\phi \approx 17\%$, confined within a sealed wedge-shaped glass cell (wedge angle $\approx 0.16°$; see Fig. S1(a) in the Supplemental Material (SM) [33]). The colloidal particles and glass walls are negatively charged in the solvent, interacting approximately via a hard-core repulsive Yukawa potential described by $u(r) = \alpha \exp[-\kappa\sigma(r/\sigma - 1)]/(r/\sigma)$ for $r > \sigma$, where r is the interparticle distance, and σ is the colloid diameter (1.5 μm). The range and strength of the repulsive interaction depend on the Debye screening length, $1/\kappa$, and a parameter, α, respectively, which are experimentally controlled by adding tetrabutylammonium bromide salt or applying ultrasonication to the solvent [5,36]. Here $\alpha = \{Q^2/\sigma[1 + (\kappa\sigma/2)]^2\epsilon_s\}$, where Q is the colloidal particles' surface charges, and ϵ_s is the dielectric constant of solvent [30,36,37]. The phase diagram of the bulk system measured in our experiments is shown in Fig. S1(b) in SM [33].

To observe the 3D structure of thin films and precisely determine each particle's position and movement, we use a Leica-SP8 fast confocal microscope coupled with particle tracking methods [38,39]. We use the 3D bond orientational order parameters, Q_l and W_l (see SM [33] for their definitions), to identify possible 3D crystalline structures (bcc type, fcc type, and hcp type) [31,32,40–43]. The criteria for identifying these structures are as follows: bcc type ($Q_6 > 0.3$, $W_6 > 0$), fcc type ($Q_6 > 0.3$, $W_6 < 0$, $W_4 < 0$), and hcp type ($Q_6 > 0.3$, $W_6 < 0$, $W_4 > 0$).

When $\kappa\sigma \approx 2.0$, the bcc crystal exhibits stability in 3D bulk configurations. As expected, when $N > 13$, we observe the prevalence of the bcc-type structure, where the $(1,1,0)_{bcc}$ plane is parallel to the smooth wall. This orientation is favored due to entropy constraints imposed by wall-induced layering [31,32]. Intriguingly, stronger confinement leads to crystalline symmetries that differ from the bulk bcc structure. For $2 \leq N \leq 13$, we observed three types of multilayered structures: stacked rhombic layers ($2 \leq N \leq 4$), fcc type [$(1,1,1)fcc\|$ wall] or $N\triangle$ structure ($2 \leq N \leq 13$), and the standard bcc-type structure [$N \geq 4$, $(1,1,0)bcc\|$ wall], illustrated in Figs. 1(a)–1(c) and 1(g). The rhombic layer features a rhombus angle ranging from 80° to 90°, while the $(1,1,1)fcc$ layer and the $(1,1,0)bcc$ layer exhibit characteristic rhombus angles of 60° and 70°, respectively [Fig. S1(e) in SM [33]]. The Nrhombic structure possesses $W_6 > 0$ and closely resembles a bcc form with a deformed $(1,0,0)_{bcc}$ plane parallel to the wall [Fig. S2(a) in SM [33]].

Interestingly, with an increase in the wall-wall separation, Z, three distinct phase reentrance behaviors emerge among these thin-film solids: $(N-1)\triangle \rightarrow N$rhombic $\rightarrow N\triangle$ for $2 \leq N \leq 3$ [Fig. 1(a)], Nrhombic $\rightarrow Nbcc \rightarrow Nfcc \rightarrow (N+1)bcc$ for $N = 4$ [Fig. 1(b)], and $Nfcc \rightarrow (N+1)bcc \rightarrow (N+1)fcc$ for $5 \leq N < 13$ [Fig. 1(c)], as shown in Fig. 1(g). Note that the $N = 5$ rhombic structure is not robustly found in experiments. The reentrances observed for $N \leq 4$ mirror those found in previous studies of charged colloids at lower density [19]. Notably, the reentrances for $N \geq 5$ represent a novel experimental result for confined colloidal thin films.

To validate these reentrance behaviors, we conducted Monte Carlo simulations in the NPT ensembles [44]. Remarkably, at comparable effective temperatures in units of the melting temperature T_m of bulk samples, our simulation results at $\kappa\sigma = 2.0$ closely align with experimental observations, evident in the comparable 2D structures [Figs. 1(a)–1(c)] and $g(r)_{2D}$ profiles [Figs. 1(d)–1(f)]. Consistent with previous studies [10,13], we find the noselike phase boundary of these reentrance structures using k_BT/α and Z as the control parameters (Fig. S3(a) in SM [33]). The confinement induces a nonmonotonic modulation in the Z-dependent Gibbs free energy (N_p particles), enthalpy (H/N_pk_BT), and entropy (S/N_pk_B), with $G(Z)$ exhibiting local minima and maxima, as shown by a typical 3rhombic $\rightarrow 3\triangle$ transition [see Fig. S3(c) in SM [33]] and a typical $5fcc \rightarrow 6bcc \rightarrow 6fcc$ reentrance [see Fig. S3(d) in SM [33]].

We explore the $\kappa\sigma$ dependence of reentrance behaviors within our accessible range, $\kappa\sigma \geq 2.0$. As $\kappa\sigma$ increases up to $\kappa\sigma \approx 5.0$, the fcc crystal becomes 3D bulk-stable in our low-density samples ($\phi \approx 0.17$), and we begin to observe $N\square$ [$(100)_{fcc}\|wall$] structures [Fig. S3(b) in SM [33]]. We characterize the confinement-induced phase reentrances
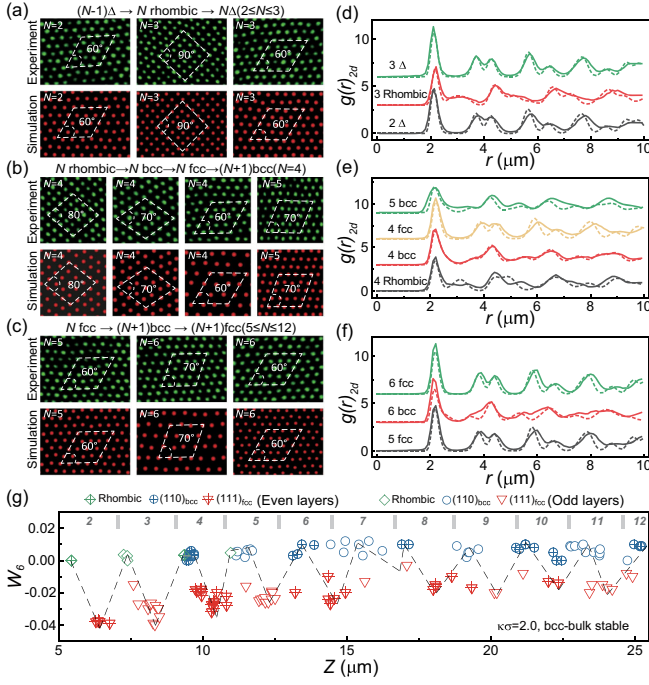
FIG. 1. Phase reentrance behaviors induced by confining low-density charged colloidal samples. (a)–(c) Illustration of typical layered structures parallel to the wall with an increase in the wall-wall separation Z. These layered structures are categorized based on the rhombus angle θ of the particle layer's 2D lattice structure: fcc type ($\theta = 60°$, $N\triangle$, or $Nfcc$ with $(111)_{fcc}\|wall$), bcc type ($\theta = 70°$, $Nbcc$ with $(110)_{bcc}\|wall$), and rhombic type ($80° < \theta < 90°$ and $W_6 > 0$, deformed bcc type with $(100)_{bcc}\|wall$). Note that the particle positions fluctuate, and we draw white dashed rhombus with specified angle to facilitate comparison. Three types of reentrance behaviors are observed: $(N-1)\triangle \rightarrow N$rhombic $\rightarrow N\triangle$ when $2 \leq N \leq 3$ in (a), Nrhombic $\rightarrow Nbcc \rightarrow Nfcc \rightarrow (N+1)bcc$ when $N = 4$ in (b), and $Nfcc \rightarrow (N+1)bcc \rightarrow (N+1)fcc$ when $5 \leq N < 13$ in (c). Simulation results (bottom panels) agree well with experiments (top panels). (d)–(f) $g(r)_{2D}$ corresponding to each structure shown in (a)–(c), respectively. The simulation results (dashed lines) also agree well with the experiment ones (solid lines). (g) Z-dependent reentrance behaviors in experiments at $\kappa\sigma \approx 2.0$. Rhombic and bcc-type structures have positive W_6. fcc-type structures have negative W_6. Different symbols are used for N and $N+1$ layers due to the possible coexistence.

using two parameters, Z/N and N [refer to Figs. 2(a) and 2(b)]. $D = Z/N$ denotes the average lattice spacing along the z direction [refer to Figs. 2(c) and 2(h)]. Here, we note that these parameters, N and D, do not serve as experimental control parameters; instead, they characterize the crystal formed under confinement.

Notably, we can classify the $\kappa\sigma$-dependent reentrance behaviors into two categories: (1) the $Nfcc \rightarrow (N+1)bcc \rightarrow (N+1)fcc$ class ($2 \leq N < 13$) when bcc is 3D bulk-stable (see also Fig. 1), e.g., at $\kappa\sigma \approx 2.0$ [see Fig. 2(a)], and (2) the $N\square \rightarrow N\triangle \rightarrow (N+1)\square$ class
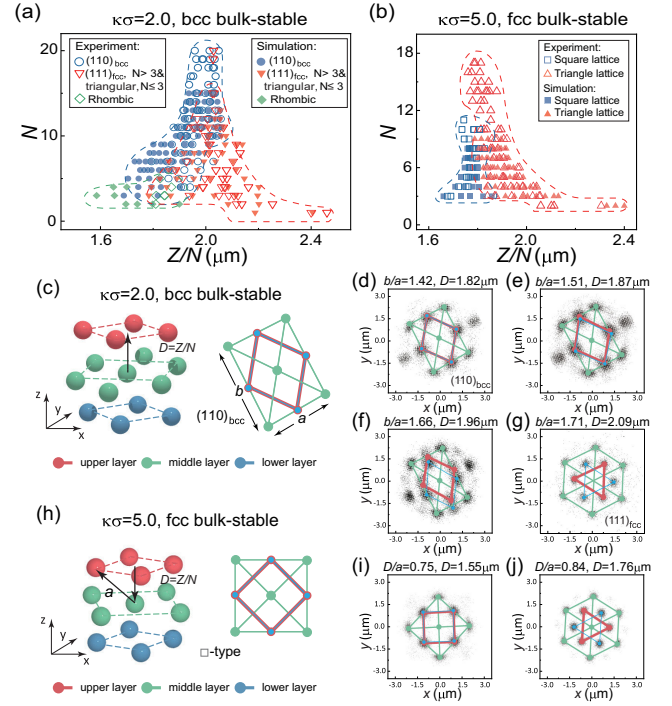

FIG. 2. Phase diagrams for the two categories of constraint-induced reentrances and the distinct 3D characters of reentrance structures. (a) The phase diagram for bcc bulk-stable systems ($\kappa\sigma \approx 2.0$) in the $(Z/N, N)$ parameter space. (b) The phase diagram for fcc bulk-stable systems ($\kappa\sigma \approx 5.0$) in the $(Z/N, N)$ parameter space. Experiments agree well with simulations in (a) and (b). (c) 3D view of the bcc-type constrained structure and illustration of its geometric parameters, D, b, and a. Note that $D = Z/N$. b and a are the unit vector lengths of the rectangle cell regarding the deformed $(110)_{bcc}$ plane. (d)–(g) Illustration of the continuous structural transformation from bcc type to fcc type at $\kappa\sigma \approx 2.0$ and $N = 4$. Scatter plots (gray clouds) are 2D projections of the solid phase's 3D structure under thermal fluctuation. Note that the upper and lower layers deform in opposite directions. (h) 3D view of the $N\square$-type structures at $\kappa\sigma \approx 5.0$. (i),(j) Illustration of the sharp structural transition from $N\square$ to $N\triangle$.

($2 \leq N < 11$) when fcc is 3D bulk-stable, e.g., at $\kappa\sigma \approx 5.0$ [see Fig. 2(b) and Fig. S1(d) in SM [33]].

The phase reentrance behavior of our low-density samples shown in Fig. 2(b) is similar to that observed in dense hard-sphere systems [7–10], which is fcc bulk-stable. With the increase of N, the variation of Z/N diminishes, and the above two reentrance behaviors vanish around $N \approx 13$ [Fig. 2(a) and Fig. S1(d) in SM [33]] and $N \approx 11$ [Fig. 2(b) and Fig. S1(d) in SM [33]], respectively. Moreover, the Nrhombic structure in Fig. 2(a) ($\kappa\sigma \approx 2.0$) with $W_6 > 0$ suggests that its 3D structure belongs to the bcc class. In contrast, the $N\square$ structure in Fig. 2(b) ($\kappa\sigma \approx 5.0$) as $W_6 < 0$, indicating that its 3D structure belongs to the fcc class [see Fig. S2(d) in SM [33]].

For $N < 10$, the presence of fcc-type structure at $\kappa\sigma \approx 2.0$ and the absence of bcc-type structure at $\kappa\sigma \approx 5.0$
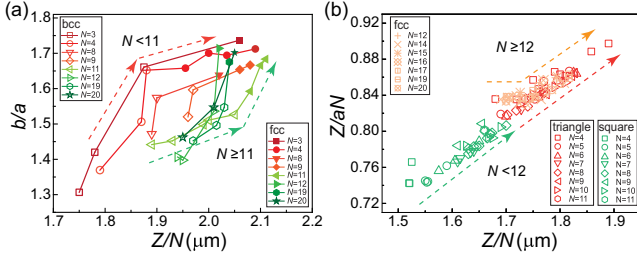
FIG. 3.   Illustration of the distinct modes of structure variation adaptive to the confinement. (a) Two different modes adaptive to the confinement operative when $N < 11$ and $N \geq 11$ in bcc bulk-stable system ($\kappa\sigma \approx 2.0$). We use the $(b/a, Z/N)$ parameter space to illustrate the differences. Note the different trends of b/a with an increase in Z/N for the two modes are schematically illustrated by red-dashed and green-dashed arrows. (b) Another two modes adaptive to the confinement operative when $N \leq 12$ and $N > 12$ in fcc bulk-stable system ($\kappa\sigma \approx 5.0$). Besides the $Z/Na \propto Z/N$ response, we can see that a new $Z/Na \approx 0.84$ branch emerges when $N \geq 12$.

suggest that a strong geometric constraint promotes fcc-type structure. Stronger confinement could also lead to a larger magnitude of the 3D structure variation, as indicated by the significant abnormal variation of Z/N at the low N in Figs. 2(a) and 2(b). This observation suggests the larger lattice deformation along the z direction for a stronger geometric constraint, for instance, smaller N.

Adaptive to a geometric variation, the 3D structure of these thin-film states deviates from the stable crystalline structure in the bulk [5,31]. These deviations may influence the stability of reentrance structures and the transformation pathways among them. However, systematic experimental measurements of these deviations have not been performed previously. We use a projection method to precisely determine the 3D structures of the thin films [26,32]. This method generates a 3D probability distribution of the solid structure under thermal fluctuations. The core of each distribution patch is identified as the average lattice position of the crystalline structure.

For the bcc-type structure at $\kappa\sigma \approx 2.0$ [Fig. 2(c)], we observe an elongation and a bidirectional slip of the $(110)_{bcc}$ plane parallel to the wall. This is evident in the characterization of the ratio, b/a, with respect to Z/N ($N = 4$) in Figs. 2(d)–2(g), where b and a are the unit vector lengths of the rectangular cell concerning the deformed $(110)_{bcc}$ plane. An ideal $(110)_{bcc}$ plane has $b/a = \sqrt{2}$, whereas an ideal hexagonal plane has $b/a = \sqrt{3}$. This continuous structural variation from bcc type to fcc type in thin-film systems could provide the lattice structure with a broad adjustment range. In contrast, the fourfold symmetry is well maintained in the $\square$ phase at $\kappa\sigma \approx 5.0$ [Fig. 2(h)], resulting in a sharp transition from $\square$ to $\triangle$ as Z/N increases [Figs. 2(i) and 2(j)].

The constraint-induced reentrance behaviors disappear around $N \approx 13$ and $N \approx 11$ in bcc bulk-stable and fcc

bulk-stable systems, respectively. These values can be considered as thermodynamic "magic layer numbers," denoted as N_c, distinguishing "thin" and "thick" film regimes. Beyond these thresholds, the amplitude of the free-energy oscillation induced by the confinement becomes too small to induce a phase change. Next, we explore another N-dependent behavior observed in thin-film systems, focusing on soft mechanical (kinetic) responses to confinement. Through an examination of the solids' deformation modes in relation to confinement, we identify a constraint-to-bulk transition at a characteristic layer number, denoted as N_k.

In bcc bulk-stable systems ($\kappa\sigma \approx 2.0$), we observe two distinct lattice deformation modes below and above $N \approx 11$, clearly distinguished in the parameter space $(b/a, Z/N)$, as depicted in Fig. 3(a). Under intense confinement ($N < 11$), there is a pronounced increase in b/a with a slight rise in Z/N in the bcc-type range (red open symbols), followed by a comparatively modest increase in the fcc-type range (red filled symbols), as indicated by the two dashed red arrows in Fig. 3(a). The initial bcc regime confirms that the elongation of the $(110)_{bcc}$ plane parallel to the wall is highly sensitive to gap variations [also evident in Figs. 2(d)–2(g)], revealing a mechanically unstable mode along specific directions. Conversely, within the fcc regime, a layered structure resembling the $(111)_{fcc}$ plane remains relatively stable against gap changes due to layering-induced stabilization [28,45,46], suggesting a predominant influence of interface energy.

In contrast, we find the opposite trend of the structure variation for $N \geq 11$, as illustrated by the other two dashed green arrows in Fig. 3(a). For $N \geq 11$, the first regime, characterized by a small slope, suggests enhanced stability of the $(110)bcc$ plane against gap changes. On the other hand, the second regime, characterized by a steeper slope, indicates a mechanically unstable mode of the $(111)_{fcc}$ plane governing the fcc-to-bcc transition. The emergence of the bulk transition mode is further substantiated by the onset of an ideal bcc structure at $N \geq 11$, as evidenced by the convergence of $\rho(W_6)$ peak positions with respect to the variations in Z/N and N in Figs. S2(b) and (c), respectively. Thus, these two distinct modes reflect two regimes with interface-energy-dominated stability and bulk elastic-energy-dominated stability.

In fcc bulk-stable systems ($\kappa\sigma \approx 5.0$), the $\square$-to-$\triangle$ transition is pronounced. To illustrate structural deformations due to confinement, we employ the $(Z/Na, Z/N)$ parameter space. Interestingly, two distinct deformation modes persist, as illustrated by the green-dashed and red-dashed arrows in Fig. 3(b) when $N < 12$, and the orange-dashed arrow when $N \geq 12$. Examining the variation of Z/N at $N < 12$, we observe that $Z/Na \propto Z/N$ for both $\square$-type (green symbols) and $\triangle$-type (red symbols) structures, indicating that a remains approximately constant regardless of the phase reentrances. In contrast, for $N \geq 12$

(orange symbols), besides the $Z/Na \propto Z/N$ response, a $Z/Na \approx 0.84$ branch emerges around $Z/N \approx 1.73$ μm, as indicated by the two-sloped orange-dashed arrows in Fig. 3(b). The initiation of a $Z/Na = 0.84$ branch for $N \geq 12$ suggests the conservation of an ideal 3D fcc-type orientational order against a slight change in the lattice constant. This behavior is absent under stronger confinement, as supported by the convergence of $\rho(W_6)$ peak positions at $N \geq 12$ concerning the variation of Z/N and N, as shown in Figs. S2(e) and (f) in SM [33], respectively. Therefore, these two mechanical (kinetic) responses here reflect the distinctive characteristics of strongly confined and weakly confined systems.

In summary, combining experiments and simulations in charged colloidal systems, we have revealed two categories of phase-reentrance behaviors induced by geometric constraints below a characteristic layer number, N_c. These categories include one characteristic of bcc bulk-stable systems and another characteristic for fcc bulk-stable systems. Indeed, the exact reentrance behaviors should be determined by the free-energy landscape of the system, such as free energies of multiple solid structures besides the stable one [10,13,19]. When the long-range interaction dominates (e.g., $\kappa\sigma \leq 1.0$, $k_B T/\alpha = 0.01$, and $\phi = 0.17$), the fcc-type reentrance structures are absent [Fig. S3(b) in SM [33]]. When the long-range interaction competes with the entropic effect due to the hard-core interaction (e.g., $\kappa\sigma = 2.0$, $k_B T/\alpha \ll 0.01$, and $\phi = 0.5$), we may expect the reentrance of bcc-type structure even though fcc is bulk-stable. Note that these two cases are usually inaccessible in colloidal experiments. More importantly, we have identified a transition in the solid deformation mode of a thin-film state between interface-energy and bulk-energy dominance: below a critical layer number N_k, geometric constraints generate unique soft deformation modes adaptive to the confinement. These characteristics under strong confinement set them apart from the 3D bulk response. For example, in bcc bulk-stable systems, a strong geometric constraint makes a thin-film bcc state more deformable, whereas the surface layering effect enhances stability in a thin-film fcc state. In contrast, in fcc bulk-stable systems, a strong geometric constraint induces significant configurational change but with only slight density variation. These diverse observations suggest that unexpected phase behaviors, leading to novel applications, can emerge in strongly confined systems, such as nanoscale architectures. Therefore, the adjustment of such structures—unattainable in bulk—through soft or long-range interactions represents a new paradigm for exploration in nanoscience.

*These authors contributed equally to this work.
†Corresponding author: r.ni@ntu.edu.sg
‡Corresponding author: tanaka@iis.u-tokyo.ac.jp
§Corresponding author: tanpeng@fudan.edu.cn

[1] T. Narayanan and K. Anil, Reentrant phase transitions in multicomponent liquid mixtures, Phys. Rep. 249, 135 (1994).

[2] P. Pieranski, L. Strzelecki, and B. Pansu, Thin colloidal crystals, Phys. Rev. Lett. 50, 900 (1983).

[3] K. Binder, Spinodal decomposition in confined geometry, J. Non-Equilib. Thermodyn. 23, 1 (1998).

[4] C. Bechinger, Colloidal suspensions in confined geometries, Curr. Opin. Colloid Interface Sci. 7, 204 (2002).

[5] Y. Chen, Z. Yao, S. Tang, H. Tong, T. Yanagishima, H. Tanaka, and P. Tan, Morphology selection kinetics of crystallization in a sphere, Nat. Phys. 17, 121 (2021).

[6] M. Schmidt and H. Löwen, Freezing between two and three dimensions, Phys. Rev. Lett. 76, 4552 (1996).

[7] M. Schmidt and H. Löwen, Phase diagram of hard spheres confined between two parallel plates, Phys. Rev. E 55, 7228 (1997).

[8] S. Neser, C. Bechinger, P. Leiderer, and T. Palberg, Finite-size effects on the closest packing of hard spheres, Phys. Rev. Lett. 79, 2348 (1997).

[9] R. Zangi and S. A. Rice, Nature of the transition from two-to three-dimensional ordering in a confined colloidal suspension, Phys. Rev. E 61, 660 (2000).

[10] A. Fortini and M. Dijkstra, Phase behaviour of hard spheres confined between parallel hard plates: Manipulation of colloidal crystal structures by confinement, J. Phys. Condens. Matter 18, L371 (2006).

[11] M. Kahn, J.-J. Weis, C. N. Likos, and G. Kahl, Ordered equilibrium structures in soft matter systems between two and three dimensions, Soft Matter 5, 2852 (2009).

[12] F. Ramiro-Manzano, E. Bonet, I. Rodriguez, and F. Meseguer, Layering transitions in colloidal crystal thin films between 1 and 4 monolayers, Soft Matter 5, 4279 (2009).

[13] E. C. Oğuz, M. Marechal, F. Ramiro-Manzano, I. Rodriguez, R. Messina, F. J. Meseguer, and H. Löwen, Packing confined hard spheres denser with adaptive prism phases, Phys. Rev. Lett. 109, 218301 (2012).

[14] B. Liu, T. H. Besseling, A. van Blaaderen, and A. Imhof, Confinement induced plastic crystal-to-crystal transitions in rodlike particles with long-ranged repulsion, Phys. Rev. Lett. 115, 078301 (2015).

[15] E. C. Oğuz, R. Messina, and H. Löwen, Multilayered crystals of macroions under slit confinement, J. Phys. Condens. Matter 21, 424110 (2009).

[16] R. Messina and H. Löwen, Reentrant transitions in colloidal or dusty plasma bilayers, Phys. Rev. Lett. **91**, 146101 (2003).

[17] E. C. Oğuz, R. Messina, and H. Löwen, Crystalline multilayers of the confined Yukawa system, Europhys. Lett. **86**, 28002 (2009).

[18] A. B. Fontecha, H. Joachim Schöpe, H. König, T. Palberg, R. Messina, and H. Löwen, A comparative study on the phase behaviour of highly charged colloidal spheres in a confining wedge geometry, J. Phys. Condens. Matter **17**, S2779 (2005).

[19] E. C. Oğuz, A. Reinmüller, H. J. Schöpe, T. Palberg, R. Messina, and H. Löwen, Crystalline multilayers of charged colloids in soft confinement: Experiment versus theory, J. Phys. Condens. Matter **24**, 464123 (2012).

[20] I. Schweigert, V. Schweigert, and F. Peeters, Enhanced stability of the square lattice of a classical bilayer Wigner crystal, Phys. Rev. B **60**, 14665 (1999).

[21] A. M. Alsayed, M. F. Islam, J. Zhang, P. J. Collings, and A. G. Yodh, Premelting at defects within bulk colloidal crystals, Science **309**, 1207 (2005).

[22] Y. Peng, Z. Wang, A. M. Alsayed, A. G. Yodh, and Y. Han, Melting of colloidal crystal films, Phys. Rev. Lett. **104**, 205703 (2010).

[23] Z. Wang, F. Wang, Y. Peng, Z. Zheng, and Y. Han, Imaging the homogeneous nucleation during the melting of superheated colloidal crystals, Science **338**, 87 (2012).

[24] Y. PengF. Wang, Z. Wang, A. M. Alsayed, Z. Zhang, A. G. Yodh, and Y. Han, Two-step nucleation mechanism in solid–solid phase transitions, Nat. Mater. **14**, 101 (2015).

[25] B. Li, F. Wang, D. Zhou, Y. Peng, R. Ni, and Y. Han, Modes of surface premelting in colloidal crystals composed of attractive particles, Nature (London) **531**, 485 (2016).

[26] M. Li, Z. Yue, Y. Chen, H. Tong, H. Tanaka, and P. Tan, Revealing thermally-activated nucleation pathways of diffusionless solid-to-solid transition, Nat. Commun. **12**, 4042 (2021).

[27] Y. Peng, W. Li, F. Wang, T. Still, A. G. Yodh, and Y. Han, Diffusive and martensitic nucleation kinetics in solid-solid transitions of colloidal crystals, Nat. Commun. **8**, 14978 (2017).

[28] K. Watanabe, T. Kawasaki, and H. Tanaka, Structural origin of enhanced slow dynamics near a wall in glass-forming systems, Nat. Mater. **10**, 512 (2011).

[29] U. Gasser, E. R. Weeks, A. Schofield, P. Pusey, and D. Weitz, Real-space imaging of nucleation and growth in colloidal crystallization, Science **292**, 258 (2001).

[30] P. Tan, N. Xu, and L. Xu, Visualizing kinetic pathways of homogeneous nucleation in colloidal crystallization, Nat. Phys. **10**, 73 (2014).

[31] S. Arai and H. Tanaka, Surface-assisted single-crystal formation of charged colloids, Nat. Phys. **13**, 503 (2017).

[32] Q. Gao et al., Fast crystal growth at ultra-low temperatures, Nat. Mater. **20**, 1431 (2021).

[33] See Supplemental Material at http://link.aps.org/supplemental/10.1103/PhysRevLett.132.018202 for supportive information and results, which includes Refs. [34,35].

[34] D. Frenkel and A. J. C. Ladd, New Monte Carlo method to compute the free energy of arbitrary solids. Application to the FCC and HCP phases of hard spheres, J. Chem. Phys. **81**, 3188 (1984).

[35] D. Frenkel and B. Smit, *Understanding Molecular Simulation: From Algorithms to Applications* (Elsevier, New York, 2001), Vol. 1.

[36] M. E. Leunissen, C. G. Christova, A.-P. Hynninen, C. Patrick Royall, A. I. Campbell, A. Imhof, M. Dijkstra, R. van Roij, and A. van Blaaderen, Ionic colloidal crystals of oppositely charged particles, Nature (London) **437**, 235 (2005).

[37] A.-P. Hynninen and M. Dijkstra, Phase diagrams of hard-core repulsive Yukawa particles, Phys. Rev. E **68**, 021407 (2003).

[38] J. C. Crocker and D. G. Grier, Methods of digital video microscopy for colloidal studies, J. Colloid Interface Sci. **179**, 298 (1996).

[39] M. Bierbaum, B. D. Leahy, A. A. Alemi, I. Cohen, and J. P. Sethna, Light microscopy at maximal precision, Phys. Rev. X **7**, 041007 (2017).

[40] P. J. Steinhardt, D. R. Nelson, and M. Ronchetti, Bond-orientational order in liquids and glasses, Phys. Rev. B **28**, 784 (1983).

[41] P.-R. Wolde, M. J. Ruiz-Montero, and D. Frenkel, Simulation of homogeneous crystal nucleation close to coexistence, Faraday Discuss. **104**, 93 (1996).

[42] W. Lechner and C. Dellago, Accurate determination of crystal structures based on averaged local bond order parameters, J. Chem. Phys. **129**, 114707 (2008).

[43] W. Mickel, S. C. Kapfer, G. E. Schröder-Turk, and K. Mecke, Shortcomings of the bond orientational order parameters for the analysis of disordered particulate matter, J. Chem. Phys. **138**, 044501 (2013).

[44] K. Sankaewtong, Q.-l. Lei, and R. Ni, Self-assembled multilayer simple cubic photonic crystals of oppositely charged colloids in confinement, Soft Matter **15**, 3104 (2019).

[45] A. Page and R. Sear, Freezing in the bulk controlled by prefreezing at a surface, Phys. Rev. E **80**, 031605 (2009).

[46] M. Dijkstra and R. van Roij, Entropic wetting in colloidal suspensions, J. Phys. Condens. Matter **17**, S3507 (2005).